Research Article | Vol. 30, No. 9 / 25 Apr 2022 / Optics Express 14518
Optics EXPRESS

Ultrafast all-optical phase switching enabled by epsilon-near-zero materials in silicon

JUAN NAVARRO-ARENAS, JORGE PARRA, AND PABLO SANCHIS*

Nanophotonics Technology Center, Universitat Politècnica de València, Camino de Vera s/n, 46022 Valencia, Spain
*pabsanki@ntc.upv.es

Abstract: Transparent conducting oxides (TCOs) have emerged as both particularly appealing epsilon-near-zero (ENZ) materials and remarkable candidates for the design and fabrication of active silicon nanophotonic devices. However, the leverage of TCO's ultrafast nonlinearities requires precise control of the intricate physical mechanisms that take place upon excitation. Here we investigate such behavior for ultrafast all-optical phase switching in hybrid TCO-silicon waveguides through numerical simulation. The model is driven from the framework of intraband-transition-induced optical nonlinearity. Transient evolution is studied with a phenomenological two-temperature model. Our results reveal the best compromise between energy consumption, insertion losses and phase change per unit length for enabling ultrafast switching times below 100 fs and compact active lengths in the order of several micrometers.

1. Introduction

A key factor in digital logic circuit performance is switching speed. Today's applications require high switching speed (<100 ns) to meet the requirement of ultra-high-density information processing and storage [1]. In traditional electronics, the RF bandwidth and energy consumption of a switching element is fundamentally limited by the RC product which, in CMOS electronics, is proportional to the scale of the gate capacitor. During the last decades, foremost enhancements in the performance of switching electronics have come largely through the engineering effort to reduce the size of transistors. At present, however, there are increasing concerns that we are approaching the end of our ability to scale such electronic components. In this context, all-optical switching is regarded as a potential technology that may play a role in boosting a new generation of ultrafast all-optical based networks and photonic central processing units [2].

There are multiple CMOS compatible photonic technologies and solid-state systems that take advantage of light-matter interactions for enabling ultra-fast all-optical switching [3,4]. The most prevalent all-optical switching mechanism consists of a pump-induced nonlinear complex refractive-index change—affecting both n_2 coefficient for pure-phase switching, β for amplitude switching, or both—but other effects, such as photonic-bandgap (PBG) or nonlinear polarization rotation (NPR), can also be exploited. Under this approach, the pump signal is used to switch ON/OFF the resonance of photonic crystals [5–7]; surface plasmon polaritons (SPPs) [8,9]; micro-ring resonators [10,11]; metamaterials [12]; or to induce a transition in hybrid waveguides loaded with phase-change materials [13,14]. However, although over the last few decades integrated optics have reached significant milestones with the development and optimization of the aforementioned photonic structures and nonlinear materials, such devices struggle to meet the requirements of high speed and high-capacity information processing [3]. Thereby, the introduction of novel physics effects in silicon photonics can be crucial to successful innovation. Indeed, in 2016 Alam et al. showed that indium tin oxide (ITO), a commercially available transparent conducting oxide (TCO) widely used in microelectronics,

#454181 https://doi.org/10.1364/OE.454181
Journal © 2022 Received 24 Jan 2022; revised 23 Mar 2022; accepted 29 Mar 2022; published 18 Apr 2022

Optics EXPRESS

exhibits a large—unity order—nonlinear response linked to the intriguing effect of epsilon-near-zero (ENZ) [15]. The ENZ occurs when the real permittivity becomes close to zero resulting in extraordinary enhancement of local electric field [16] and extreme optical nonlinear effects [17–19]. Comparable ENZ effects have also been measured in other TCO bulk films such as cadmium oxide [20] and zinc oxide [21]. In the subsequent years, the integration of TCOs in photonic devices was demonstrated for enabling ultrafast modulations of their complex refractive index at telecom wavelengths [22]. Depending on their carrier concentration, and unlike noble metals, TCOs can be considered low-loss materials, bringing the possibility to explore new concepts based on plasmonic effects. Moreover, thin film technology based on TCOs have the added possibility of introducing important modifications in the material's properties, namely the electron mobility and the carrier concentration, during the fabrication time through layer growth conditions and post-treatment. In this way, sparsely doped TCOs can produce a quasi-neutral region of charge carrier concentration between 10^{20} and 10^{21} cm^{-3} [23], allowing the ENZ resonance wavelength to be fine-tuned in the third telecom window [22]. Such features have been envisaged for bringing high-performance functionalities into the silicon photonics platform such as data modulation [24,25], nanophotonic phased arrays [26], neuromorphic computing [27], or even on-chip quantum networks [28].

To date, most TCO modeling and experimental efforts based on the ENZ effect have focused on amplitude switching [24,25], and only a few works exploit changes in the real part of TCO's permittivity for enabling optical phase shifters. One possible approach relies on a floating gate configuration to electro-optically change the TCO properties through electron density tuning [29,30] rather than exploiting the intraband electronic transitions occurring when the material is excited all-optically. Indeed, to the best of our knowledge, no solution for a TCO/Si all-optical phase-switching device has yet been demonstrated, nor proposed. The emphasis on exploring large changes of the optical phase in the ENZ region with low losses constitutes the novelty of this work.

Here we present an ENZ-based all-optical phase switch built on a TCO/Si hybrid waveguide operating near the third telecom window with ultrafast switching time—tens of femtoseconds—and picojoule energy consumption. The impact of the TCO's carrier density and mobility on the performance of the switch is investigated through three-dimensional (3D) finite-difference-time-domain (FDTD) simulations. Our numerical analysis determines the best configuration to allow an optimal compromise between energy consumption, insertion losses and phase change per unit length. The manuscript is divided into five sections plus this introduction: Section 2 contains an explanation of the model utilized to tackle the changes of the TCO's dielectric function upon ultrafast excitation; in Section 3 the space of parameters of material properties and device geometry is explored to find an efficient design; constraints on how to efficiently pump the photonic structure are presented in Section 4; 3D-FDTD simulations of the optimum device are described in Section 5; finally, a concluding remark is presented.

2. Modelling of the all-optical switching mechanism in ENZ materials

The physics of ENZ materials are originated at the intraband electronic transitions, in which the electronic temperature can rise to a few thousand Kelvin, and the electrons reallocate in a non-parabolic conduction band, defining a temperature-dependent effective-mass contribution that can be unwinded in the Drude model for free electrons [31]:

$$\varepsilon = \varepsilon_\infty - \frac{\omega_p^2}{\omega^2 + i\Gamma\omega} \tag{1}$$

Optics EXPRESS

where ε_∞. is the high-frequency permittivity. The ω_p. is the plasma frequency and Γ is the damping frequency, which can be expressed in terms of:

$$\omega_p^2 = \frac{Ne^2}{\langle \mathrm{m_e^*} \rangle \varepsilon_0}; \quad \Gamma = \frac{e}{\mu \langle \mathrm{m_e^*} \rangle} \tag{2}$$

N is the carrier density, e electron charge, ε_0 is the vacuum permittivity, μ is the electron mobility, $\langle m_e^* \rangle$ is the statistically averaged effective electron mass weighted according to the Fermi–Dirac distribution f_{FD} in a Kane-type non-parabolic second-order conduction band [32], $\gamma(E) = E + CE^2$, which is an approximation commonly adopted in the context of transparent conducting oxide materials to account for the optical nonlinear effects:

$$\frac{1}{\langle m_e^* \rangle} = \frac{\int_0^\infty \frac{1}{m_D^*(E)} N_D f_{FD}\, dE}{N} \tag{3}$$

in which $N_D = \gamma^{1/2}(d\gamma/dE)(2m_0^*/\hbar^2)^{3/2}/(2\pi^2)$ is the density-of-states (DOS) and $m_D^*(E) = m_0^*\, d\gamma/dE$ is the DOS effective mass, m_0^* is the electron effective mass weighted at the conduction band minimum, E is the electron energy referenced to the band minimum, and $\hbar$ is the reduced Plank constant. Implicit dependence with the electronic temperature T_e is given by the Fermi–Dirac distribution (i.e., $f_{FD} = \{\exp[(E - E_F(T_e))/(k_B T_e)] + 1\}^{-1}$, where E_F is the Fermi level and k_B is the Boltzmann constant) of conduction electrons [33]. Since the carrier density (i.e., $N = \int_0^\infty f_{FD} N_D dE$) is conserved for intraband transitions, a functional relation between E_F and T_e can be obtained for a given value of N.

This dissipates energy through electron–phonon interactions, increasing the lattice temperature T_l, until the system reaches an equilibrium state. Such systems can be accurately described by a two-temperature model (TTM) which is a common method to describe the temperature dynamics of electrons and phonons upon ultrafast excitation in metals [31].

$$\begin{aligned} C_e \frac{\partial T_e(t)}{\partial t} &= -g_{ep}(T_e(t) - T_l(t)) + \frac{N(t)}{2\tau_{ee}(t)} \\ C_l \frac{\partial T_l(t)}{\partial t} &= g_{ep}(T_e(t) - T_l(t)) + \frac{N(t)}{\tau_{ep}(t)} \\ \frac{\partial N(t)}{\partial t} &= -\frac{N(t)}{2\tau_{ee}(t)} - \frac{N(t)}{\tau_{ep}(t)} + P(t) \end{aligned} \tag{4}$$

where C_e and C_l respective heat capacities of electron and lattice; g_{ep} is the electron-phonon coupling coefficient, a parameter that determines the rate of the energy exchange between the hot electrons and the vibrational modes of the lattice; τ_{ee} and τ_{ep} are the electron-electron and electron-lattice relaxation times. The calculations of the temperature dependence of the parameters mentioned above is done according to the model recovered from citing literature [33–36]. Moreover, N. is the fraction of energy density stored in the non-thermalized part of the electron plasma and $P(z,t) = I_0 \alpha_p(\mathrm{z,t}) \exp[-2(t/\tau_p)^2]$ is the heat source, the absorbed power density of a Gaussian-shaped pump pulse where τ_p indicates the time normalization factor that decides the pulse duration; I_0 is the peak intensity (power per unit area); and $\alpha_p(\mathrm{z,t})$ the modal absorbance.

Pump pulse and probe were assumed to propagate at the fundamental TM modes of the hybrid waveguide (with high confinement factor in the TCO layer). Such modes were calculated with the permittivity given from the extended Drude model by using a mode solver based on the Finite Element Method integrated with RSoft CAD environment from Synopsys. Once the effective index of the photonic structure was determined, the dynamical set of TTM equations were solved with a one-dimensional finite-difference time-domain (1D-FDTD) iterator implemented in Python code. In this script, the electron temperature was used as an input parameter in an

Optics EXPRESS

interpolation function that returned the value of the complex effective index. Returned values were assigned to the finite segments of the hybrid waveguide. In this way, the modal absorbance $\alpha_p(z, t)$ and phase velocity of each segment were determined and used to iterate the TTM.

The parameters used in the simulation are collected in Table 1, and correspond to a highly doped, high-mobility cadmium oxide [25]. As an additional consideration, nonlinear effects of the Si waveguide core (i.e., free-carrier effects) are neglected due to the strong light confinement in the TCO, the sub-picosecond time scale and the short propagation lengths.

Table 1. Material properties used for simulation

m_0^*	$0.16\ m_0$
ε_∞	5.6
C	$0.5\ \mathrm{eV}^{-1}$
N	$(6–8)\ 10^{20}\ \mathrm{cm}^{-3}$
μ	$(100–300)\ \mathrm{cm}^2\mathrm{V}^{-1}\mathrm{s}^{-1}$

3. Design strategy for high-performance all-optical phase switching

All-optical phase switching is attained by employing a pulsed pump and a continuous wave (CW) probe configuration that shifts the device between two low loss states with different phase velocities. The proposed all-optical phase-switching device is shown in Fig. 1 and it consists of a standard silicon-on-insulator (SOI) waveguide with a thin layer of TCO on top surrounded by a SiO_2 upper cladding. A cross-section of the waveguide structure is also shown in Fig. 2(a).

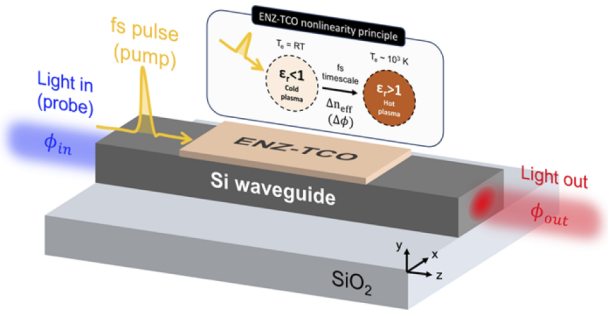

Fig. 1. Schematic of the proposed all-optical phase switch based on a TCO/Si waveguide. The TCO material absorbs the power of a TM polarized optical pump pulse so that the electronic temperature is increased and a strong modulation in the real part of the effective index is achieved whilst the change of the imaginary part is minimized. Thereby, an optical phase shift is induced in a continuous wave (CW) probe signal triggered by the pump signal.

The switching operation is achieved by transitioning the TCO film between a metal-like state and a dielectric-like state by raising the electronic temperature—which necessarily implies a change of sign in the real part of the TCO's dielectric constant function—with a TM polarized optical pump pulse. In Fig. 2(b), the optical constants at 1550 nm of the TCO with the parameters of Table 1 are calculated near the ENZ resonance, located at $T_e^{ENZ} = 5500$ K (ENZ temperature), to display this transition. The effective index of the hybrid waveguide is also calculated in Fig. 2(b) showing that, around the ENZ resonance, the imaginary part of the mode is maximal due to the enhanced modal field confinement, and that a significant phase difference can be exploited between the two states if the induced losses are carefully handled.

Optics EXPRESS

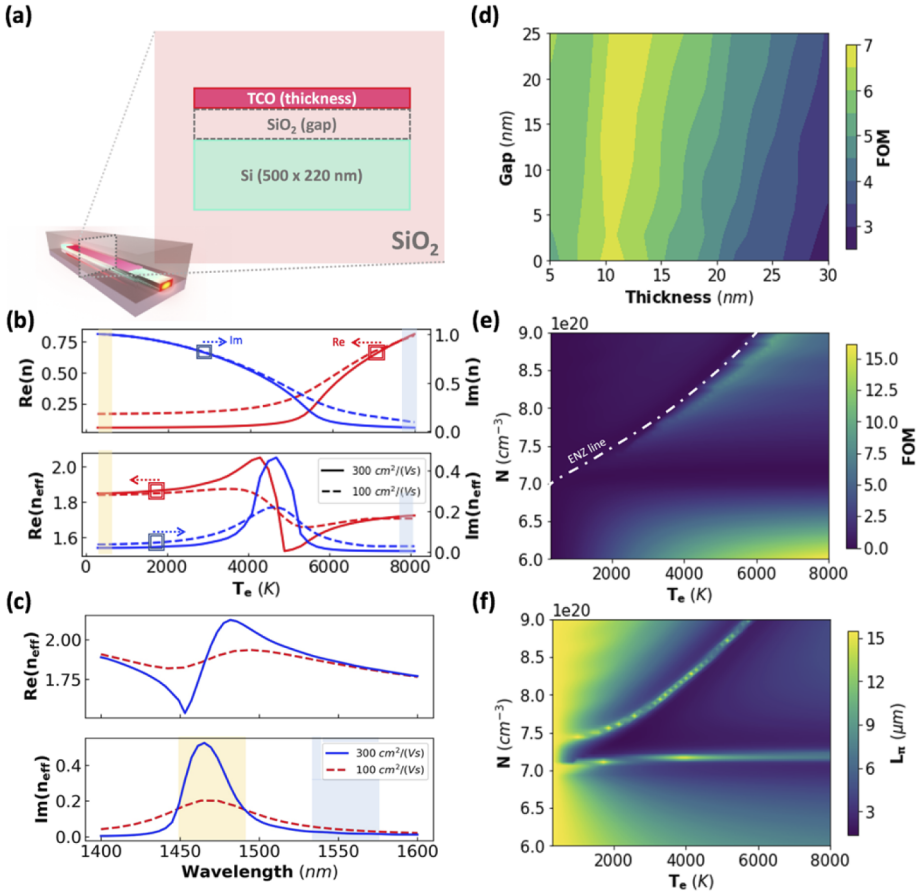

Fig. 2. (a) Cross-section of the hybrid TCO/Si waveguide. (b) TCO's optical constants as a function of the electronic temperature, calculated with the parameters of Table 1, and effective index of the hybrid waveguide at a fixed wavelength of 1550 nm for a carrier concentration of $N = 8.5 \times 10^{20}$ cm^{-3} and two different mobilities. The yellow shaded region represents the switch's OFF state; the blue shaded region represents the ON state. (c) Wavelength dependant effective index calculated for two different mobilities with fixed $N = 8.5 \times 10^{20}$ cm^{-3} at 1550 nm. The yellow shaded region shows the ENZ resonance; the blue shaded region depicts the optimal probe wavelength. (d) Contour map of the FOM to optimize the gap and TCO thickness of the hybrid waveguide taking into account a carrier concentration of $N = 8.5 \times 10^{20}$ cm^{-3} at 1550 nm. Contour map of the (e) FOM and (f) length for a π phase shift as a function of the carrier concentration and electronic temperature and $\mu = 300$ cm^{2}V^{-1}s^{-1}.

Optics EXPRESS

From the perspective of design, the two most important parameters of a TCO described by a Drude model (Eqs. 1–3) are carrier density N and mobility μ. While changing N results in blue-shifting the ENZ frequency—or increasing the ENZ temperature—, μ has an effect on the shape, linewidth and amplitude, of the temperature and wavelength response of the plasmon resonance, as it can be seen in Fig. 2(b) and Fig. 2(c), therefore affecting the modulation depth introduced by the ENZ resonance [25] and, ultimately, the switching energy E_S and the dynamics of the heating process.

The carrier density must be carefully chosen as a compromise between switching energy and insertion losses. Having an ENZ window resonant with the probe wavelength introduces high optical losses due to strong modal confinement in the lossy TCO film but, on the other side, shifting the ENZ away from the probe wavelength increases the energy required to switch between metallic and dielectric states. Accordingly, to maximize this phase difference while minimizing the losses, the shape of the ENZ resonance in the space of temperatures must be narrow. One way to achieve this is to increase the value of the electronic mobility, as it can be seen in Fig. 2(b).

Recent publications [17,25] state that TCO-based efficient phase switching can only be realized with high-mobility TCOs ($\mu > 200$ cm^{2}V^{-1}s^{-1}). The technology to produce ultra-high mobility dysprosium-doped cadmium oxide (CdO:Dy), with a maximum achievable mobility of ~500 cm^{2}V^{-1}s^{-1} for carrier concentrations in the orders magnitude of $5\times10^{20} < N < 10^{21}$ cm^{-3}, has been recently demonstrated [37]. Other potential dopants such as yttrium have also been recently explored to produce high mobility CdO but with carrier concentrations in the order of 5×10^{19} cm^{-3} to 2×10^{20} cm^{-3} [20,38]. In our model, an upper bound of 300 cm^{2}V^{-1}s^{-1} was chosen to demonstrate high-performance all-optical phase switching.

The optimal performance is achieved by analyzing the multivariable space defined by the TCO's carrier density and switching temperature. These two parameters determine the maximum phase shift ($\Delta\phi$) that the device can generate with minimal losses (IL). Thereby, a pump signal—expressed in terms of peak power, pulse width and wavelength—of minimal energy consumption must be defined to excite the TCO at the switching temperature. Moreover, this optimal configuration can be further improved by designing the device's geometrical parameters—the thickness of the TCO film and its gap with the Si waveguide—. Such a rich and intricate space of parameters can be tackled by defining the following figure of merit (FOM):

$$FOM = \frac{\Delta\phi}{IL} = \frac{1}{2}\frac{\Delta Re(n_{eff})}{Im(n_{eff})} \tag{5}$$

The effect of geometry in the complex effective index of the hybrid waveguide modes can be initially explored with fixed $N = 8.5\times10^{20}$ cm^{-3} at 1550 nm without loss of generality. The results are presented in Fig. 2(d) revealing that the best design choice constraints the TCO film thickness to 10 nm. Since the SiO_2 gap has little impact on the FOM it can be thought as a free design parameter or a tolerance against Si oxidization. On the other hand, mapping the FOM over the space of parameters of electronic temperature and carrier concentration allows to isolate the material's optimal working conditions. In Fig. 2(e), two high-FOM regions can be identified. The first one is delimited by having an $N < 7.0\times10^{20}$ cm^{-3}, which is the limiting carrier concentration that defines the ENZ temperature at 300 K for a wavelength of 1550 nm. However, the operation in this region takes no advantage of the change of sign in the dielectric constant introduced by the ENZ resonance and, hence, the attainable phase shift is comparatively low. The second region is defined by $N > 7.0\times10^{20}$ cm^{-3} and circumscribes a ridge in the FOM map formed by a stark change of $\Delta\phi$ in the vicinity of the ENZ resonance and reduced losses after crossing the ENZ resonance (see Fig. 2(b)). Higher values of N shift the ENZ resonance to higher temperatures, away from room temperature, and reduce the device's OFF state insertion

Optics EXPRESS

losses, slightly enhancing the FOM. This improvement, however, is at the cost of higher switching energies.

Considering the energy consumption argument, despite the FOM is greater in the first region, since the available pump power decays exponentially with the propagating distance, the energy required to introduce a π phase change is comparatively large, as it can be seen in the L_π map of Fig. 2(f). This entails a limitation in the allowable parameters to operate the device all-optically. Only the second region with $N > 7.0 \times 10^{20}$ cm^{-3}, together with a certain range of electronic temperatures, allows designs with compact footprints and energies consumption in the order of the picojoule. On the other hand, it should also be pointed out that excessively high carrier concentrations [37,38] or undesired carrier effects, such as interface scattering [39], may degrade the device performance through decreased mobility, especially in the case of thinner films (< 20 nm). However, the FOM would only be reduced in a linear way with respect to the mobility. In our device, for instance, a FOM of around 2 is achieved for a mobility of 100 cm^{2}V^{-1}s^{-1} compared to the values of around 7 given for μ = 300 cm^{2}V^{-1}s^{-1}.

4. Analysis of energy consumption and temporal response

The temporal dynamics following ultrafast laser excitation—pump pulse—in the TCO film can be examined with the TTM equations. The result of the simulations reveals that the hybrid waveguide can be evenly excited at high electronic temperatures (T_e > 5000 K) if the pump wavelength is carefully tuned. Indeed, if the device is operated in the $N > 7.0\ 10^{20}$ cm^{-3} region and pumped with wavelengths longer than 1550 nm, the hybrid waveguide behaves as a saturable absorber due to the resonant nature of the ENZ effect. In such situation, the pump pulse is absorbed while the electronic temperature increases, causing the ENZ resonance to redshift, until it eventually converges at the pump wavelength. The modal absorption is then decreased because the electronic temperature is higher than the ENZ (peak) temperature. Thus, when an excited portion of the waveguide is saturated, its temperature can no longer increase but the absorption of the optical pulse continues along the propagation direction, in the inner depths of the hybrid waveguide, where the TCO material rests at room temperature. In this way, a uniform distribution of electronic temperatures can be engineered in the entire length of the device by adjusting the pump wavelength, providing that the pulse carries sufficient energy.

It is worth mentioning that one advantage of working in the T_e plateau region is that the probe signal is more robust against power fluctuations of the pump signal. Additionally, the wavelength-tunable electronic temperature plateau allows multilevel all-optical switching by tuning the pump wavelength.

This complex behavior is summarized in Fig. 3(a). The energy in a 6-μm-long hybrid waveguide required to increase the electronic temperature to a certain spatially averaged value is plotted for different pump wavelengths. It can be seen that for each pump wavelength there is a saturation energy threshold. In general, this average temperature ceiling matches the ENZ temperature for that given wavelength, but the threshold power depends on the propagation length. Homogeneous distribution can be achieved with sufficiently high pump energy, as depicted in Fig. 3(b). An energy above 6 pJ is required to generate a uniform change in the TCO with a pump wavelength of 1616 nm.

The pump wavelength must be chosen in agreement with the TCO's carrier concentration as this parameter determines the ENZ room temperature and losses. A material with $N = 8.8 \times 10^{20}$ cm^{-3} presents the resonance at T_e^{ENZ}= 6000 K (λ_{ENZ} = 1550 nm). The FOM is maximized with switching temperatures from 6500 to 7100 K (λ_{ENZ} around 1600 nm), see Fig. 2(e). To determine the optimal characteristics of the pump signal, wavelength and pulse energy, the FOM is also calculated as a function of these parameters. The obtained results are depicted in Fig. 3(b). The maximum value is achieved with a pulse of 7.5 pJ at 1616 nm, which results in a phase shift of around π radians together with propagation losses of 2-3 dB.

Optics EXPRESS

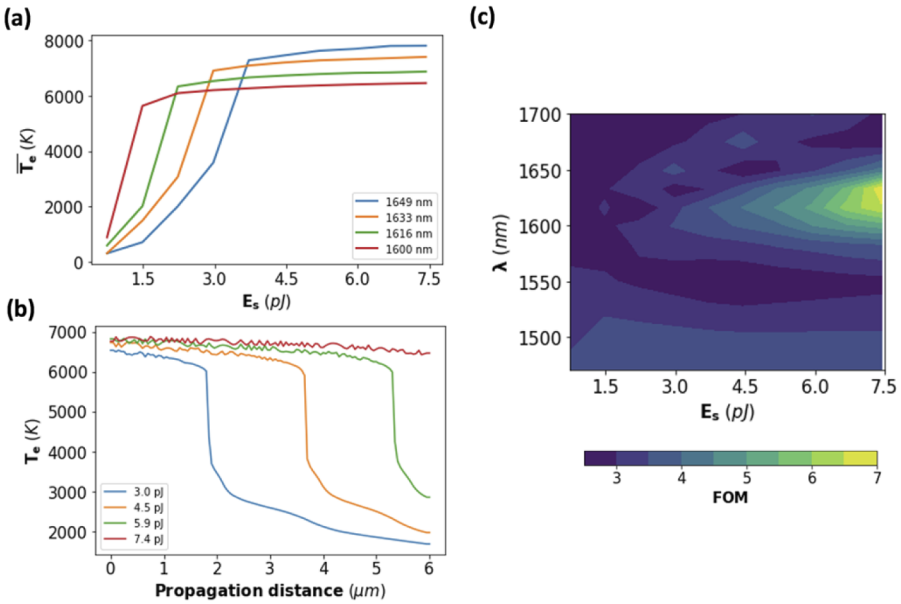

Fig. 3. Electronic temperature distribution for $N = 8.8 \times 10^{20}$ cm^{-3} and the parameters of Table 1. (a) Spatially and time averaged distributions parametrized by pump energy and pump wavelength with a fixed propagation length of 6 μm. (b) Time averaged spatial distributions parametrized by propagation distance and pump energy with a fixed pump wavelength of 1616 nm. (c) Contour map of the FOM for the pump wavelength and energy. In this simulation the pump pulse was defined by a Gaussian shape with a full width at half maximum (FWHM) of 75 fs and different pump energies. Switching energy was calculated following the usual integral definition. The electronic temperatures were calculated after the first half of the pump pulse is absorbed (shadowed areas of Fig. 4(a)) to obtain the temperature in the ON temporal window.

The TTM equations are also used to analyze the effect of pump pulse power and duration (τ_p). As shown in the results of Fig. 4(a), the TCO active layer can produce a switching window—shadowed area in the figure—with a flat T_e response. The duration of the switching window is roughly equal to the duration of the pump pulse. On the other hand, the delay between the pump pulse and the electron distribution heating, which is mediated by the electronic heat capacity in the TTM equations, defines a delayed hot-electron nonlinearity that is characteristic of physical systems such as this one [40]. After the pump pulse, the system undergoes a transient evolution until electron and phonon distributions reach thermal equilibrium [36]. In Fig. 4(a) it is demonstrated that the device can be operated with pump pulses as short as 25 fs. It is also interesting to note that the ratio between the maximum T_e achieved in the ON window and the convergence temperature, at the end of the cooling down tail of the curve, scales with the pump pulse duration. This is, in fact, another fundamental limitation of TCO-based all-optical switches. The effect is a consequence of the asymmetry between electron-electron and electron-phonon relaxation times ($\tau_{ee} << \tau_{ep}$). Electron-phonon interactions become relevant at time scales in the picosecond order while electron-electron scattering dominates in the sub-picosecond regime [41]. Therefore, when the excitation window is resonant with τ_{ep} the electron–phonon interactions intensify and the thermal equilibrium temperature, at which the hot electrons converge with the lattice, increases. Certainly, as it can be seen in Fig. 4(b), the system's equilibrium temperature tiers when the pulse duration is enlarged from values of $\tau_p < 100$ fs to a time window in the order of the picosecond. In our case, pump pulses longer than 0.2 ps lead to the thermal activation of

Optics EXPRESS

the lattice with temperatures higher than 1000 K. Simulations reveal that this effect also scales with pump pulse power but much less significantly. Since the heat capacity of the lattice is much larger than that of the electrons, entailing that the energy loss rate of the lattice is much slower, the lattice acts as a heat reservoir that delays the switch's ability to fully return to the OFF state. This behavior significantly limits the device's ON/OFF ratio, imposing a limitation in the pump pulse repetition rate in the order of tens to hundreds of picoseconds [15]. Furthermore, since the electronic temperature reaches several thousands of Kelvins, significant heat transfer towards the lattice can permanently damage the TCO film [42]. Hence, in order to operate the device with high pump powers the duration of the pulse must be kept below 200 fs regardless of peak power.

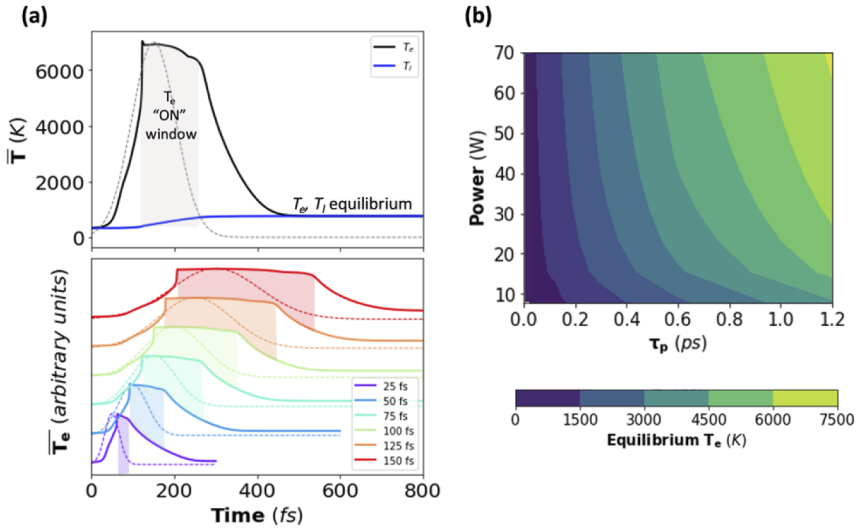

Fig. 4. (a) Electronic temperature and lattice temperature temporal distribution (black and blue continuous lines respectively) for $N = 8.8 \times 10^{20}$ cm^{-3} and excited with a Gaussian pump pulses (discontinuous lines) with a FWHM of 75 fs. The plot is extended below to show the effect of different pump pulse durations. Electronic temperatures are spatially averaged in a 6-μm hybrid waveguide. The shadowed area represents the ON state. (b) Contour map of the equilibrium temperature obtained after the absorption of one full pump pulse.

5. Optimal design and discussion

An optimized device has been designed to achieve a π-radians phase shift with a switching energy of 7.5 pJ, a footprint of 6 μm with and a switching time of 75 fs. Such a device is simulated with a rigorous 3D-FDTD method. The simulations include the coupling between the standard Si waveguide and the TCO/Si waveguide. Figure 5(a) shows the temporal response of the device in terms of phase change and loss while being excited by the pump signal. The material is switched from a low-loss, real negative permittivity hybrid-plasmonic mode, to a low-loss, positive permittivity photonic mode. The change in the sign of ε_r introduces a Fano-like resonance in the carrier's phase evolution, wherein a π radians phase shift takes place around the ENZ region.

To probe further the concept of the phase switch, the 3D spatial distribution of the E_y field, computed between the two switching states of spatially averaged T_e, is displayed in Fig. 5(b). In the OFF state, with the unexcited TCO layer resting at room temperature, the insertion (propagation plus coupling) losses are as low as 2.5 dB. In the ON state, the device is excited by the pump signal, inducing a π radians phase shift at the output of the waveguide with maximum

Optics EXPRESS

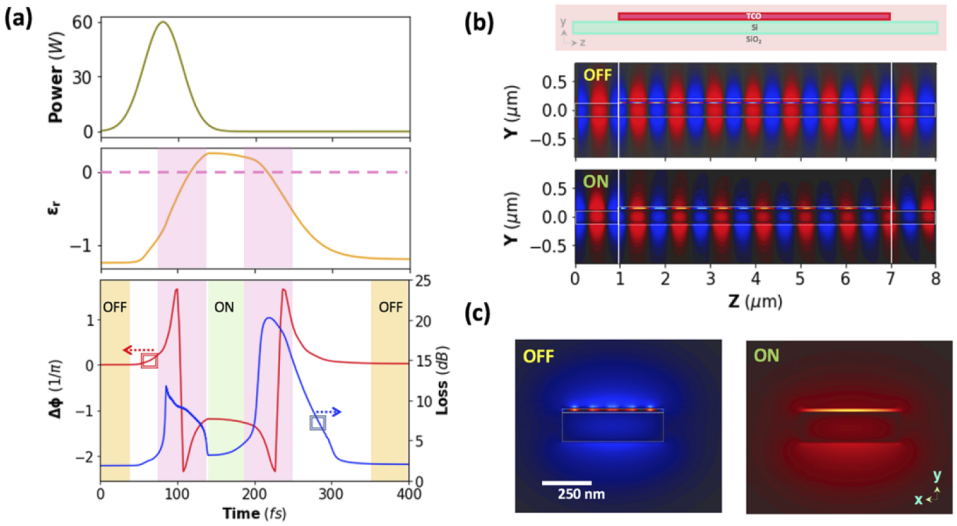

Fig. 5. (a) From top to bottom: temporal evolution of the pump pulse, real part of the TCO permittivity at 1550 nm and phase and loss response of the 6 μm-long TCO/Si waveguide. (b) *Ey* electric field obtained by a 3D-FDTD simulation in the Y-Z plane at OFF/ON states. (c) *Ey* electric field distribution of the optical mode for the ON/OFF states corresponding to complex effective indices of $n_{eff}^{OFF} = 1.80 + i0.01$ ($T_e = 300$ K) and $n_{eff}^{ON} = 1.65 + i0.02$ ($T_e = 7000$ K) respectively.

insertion losses around 4 dB. The hybrid waveguide modes are displayed in Fig. 5(c). The mode at the OFF state presents a discontinuity in the *Ey* component of the electric field that can be attributed to short-range surface plasmon-polariton (SR-SPP) nature of the waves, typically seen in the propagation along very thin metallic layers (ε_r) surrounded by dielectric materials (ε_r) [43].

6. Conclusions

A detailed analysis of the capabilities of ENZ materials based on TCOs for enabling all-optical phase switching has been provided. The complex space of parameters formed by the extended Drude model for intraband-transition-induced optical nonlinearity and the transient two-temperature model is analyzed to find the best compromise between energy consumption, insertion losses and phase change per unit length. We concluded that, in order to operate at telecom wavelengths, high mobilities and carrier concentrations above $N > 7.0 \times 10^{20}$ cm^{-3} are a design requirement. Efficient energy transfer between the pump signal and the hybrid waveguide is also explored revealing that the device acts like a saturable absorber. This property allows to produce homogeneous electronic temperature distributions in arbitrarily long hybrid waveguides. An all-optical phase-switching device is designed based on a 6-μm-long TCO/Si waveguide with ultrafast switching times, as low as 75 fs, energy consumption of a few picojoules and insertion losses around 4 dB. Such device offers an enhanced performance compared with traditional approaches based on nonlinear silicon micro-ring resonators [10,11] or photonic crystal cavities [5–7], that require long device lengths of tens or hundreds of microns, and long photon lifetimes of tens of picoseconds, to achieve high extinction ratios.

The interplay between high/low loss ENZ modes provides the highest switching efficiency in current literature [25]. Furthermore, this mechanism, limited by ultrafast electron-electron scattering rate, is among the fastest and allows to significantly reduce the insertion losses as compared with SSPs due to the optical transparency of high mobility TCOs in the third telecom

Optics EXPRESS

window. Furthermore, the assembly of such a device can be ready-made with dysprosium-doped cadmium oxide in standard SOI waveguides and its realization could pave the road towards high-performance ENZ-based all-optical phase switches compatible with the silicon platform.

Funding. Generalitat Valenciana (PROMETEO Program (Ref.2019/123)); Agencia Estatal de Investigación (FPU17/04224, ICTS-2017-28-UPV-9, PID2019-111460GB-I00).

Disclosures. The authors declare no conflicts of interest.

Data availability. Data underlying the results presented in this paper are not publicly available at this time but may be obtained from the authors upon reasonable request.

References

1. K. Ikeda, K. Suzuki, R. Konoike, S. Namiki, and H. Kawashima, "Large-scale silicon photonics switch based on 45-nm CMOS technology," Opt. Commun. **466**, 125677 (2020)..
2. Z. Chai, X. Hu, F. Wang, X. Niu, J. Xie, and Q. Gong, "Ultrafast All-Optical Switching," Adv. Opt. Mater. **5**(7), 1600665 (2017)..
3. V. Sasikala and K. Chitra, "All optical switching and associated technologies: a review," J. Opt. **47**(3), 307–317 (2018)..
4. H. Qi, X. Wang, X. Hu, Z. Du, J. Yang, Z. Yu, S. Ding, S. Chu, and Q. Gong, "All-optical switch based on novel physics effects," J. Appl. Phys. **129**(21), 210906 (2021)..
5. S. Rebhi and M. Najjar, "Hourglass nonlinear photonic crystal cavity for ultra-fast all-optical switching," Optik (Munich, Ger.) **180**, 858–865 (2019)..
6. K. Nozaki, T. Tanabe, A. Shinya, S. Matsuo, T. Sato, H. Taniyama, and M. Notomi, "Sub-femtojoule all-optical switching using a photonic-crystal nanocavity," Nat. Photonics **4**(7), 477–483 (2010)..
7. H. Nakamura, Y. Sugimoto, K. Kanamoto, N. Ikeda, Y. Tanaka, Y. Nakamura, S. Ohkouchi, Y. Watanabe, K. Inoue, H. Ishikawa, and K. Asakawa, "Ultra-fast photonic crystal/quantum dot all-optical switch for future photonic networks," Opt. Express **12**(26), 6606–6614 (2004)..
8. M. Ono, M. Hata, M. Tsunekawa, K. Nozaki, H. Sumikura, H. Chiba, and M. Notomi, "Ultrafast and energy-efficient all-optical switching with graphene-loaded deep-subwavelength plasmonic waveguides," Nat. Photonics **14**(1), 37–43 (2020)..
9. X. Zhang and J. Yang, "Ultrafast Plasmonic Optical Switching Structures and Devices," Front. Phys. **7**, 190 (2019)..
10. J. S. Pelc, K. Rivoire, S. Vo, C. Santori, D. A. Fattal, and R. G. Beausoleil, "Picosecond all-optical switching in hydrogenated amorphous silicon microring resonators," Opt. Express **22**(4), 3797–3810 (2014)..
11. M. Waldow, T. Plötzing, M. Gottheil, M. Först, J. Bolten, T. Wahlbrink, and H. Kurz, "25ps all-optical switching in oxygen implanted silicon-on-insulator microring resonator," Opt. Express **16**(11), 7693–7702 (2008)..
12. A. D. Neira, G. A. Wurtz, P. Ginzburg, and A. V. Zayats, "Ultrafast all-optical modulation with hyperbolic metamaterial integrated in Si photonic circuitry," Opt. Express **22**(9), 10987–10994 (2014)..
13. D. Tanaka, Y. Shoji, M. Kuwahara, X. Wang, K. Kintaka, H. Kawashima, T. Toyosaki, Y. Ikuma, and H. Tsuda, "Ultra-small, self-holding, optical gate switch using Ge2Sb2Te5 with a multi-mode Si waveguide," Opt. Express **20**(9), 10283–10294 (2012)..
14. K. Hallman, K. Miller, A. Baydin, S. Weiss, and R. Haglund, "Subpicosecond All-Optical Switching of 1550 nm Signals in Hybrid Silicon:VO2 Waveguides and Ring Resonators," in *14th Pacific Rim Conference on Lasers and Electro-Optics (CLEO PR 2020)* (Optical Society of America, 2020), p. C8H_3.
15. M. Z. Alam, I. De Leon, and R. W. Boyd, "Large optical nonlinearity of indium tin oxide in its epsilon-near-zero region," Science **352**(6287), 795–797 (2016)..
16. I. V. A. K. Reddy, J. M. Jornet, A. Baev, and P. N. Prasad, "Extreme local field enhancement by hybrid epsilon-near-zero–plasmon mode in thin films of transparent conductive oxides," Opt. Lett. **45**(20), 5744–5747 (2020)..
17. J. Wu, Z. T. Xie, Y. Sha, H. Y. Fu, and Q. Li, "Epsilon-near-zero photonics: infinite potentials," Photonics Res. **9**(8), 1616–1644 (2021)..
18. N. Kinsey, C. DeVault, A. Boltasseva, and V. M. Shalaev, "Near-zero-index materials for photonics," Nat. Rev. Mater. **4**(12), 742–760 (2019)..
19. O. Reshef, I. De Leon, M. Z. Alam, and R. W. Boyd, "Nonlinear optical effects in epsilon-near-zero media," Nat. Rev. Mater. **4**(8), 535–551 (2019)..
20. S. Saha, B. T. Diroll, J. Shank, Z. Kudyshev, A. Dutta, S. N. Chowdhury, T. S. Luk, S. Campione, R. D. Schaller, V. M. Shalaev, A. Boltasseva, and M. G. Wood, "Broadband, High-Speed, and Large-Amplitude Dynamic Optical Switching with Yttrium-Doped Cadmium Oxide," Adv. Funct. Mater. **30**(7), 1908377 (2020)..
21. E. G. Carnemolla, V. Bruno, L. Caspani, M. Clerici, S. Vezzoli, T. Roger, C. DeVault, J. Kim, A. Shaltout, V. Shalaev, A. Boltasseva, D. Faccio, and M. Ferrera, "Giant nonlinear frequency shift in epsilon-near-zero aluminum zinc oxide thin films," in 2018 *Conference on Lasers and Electro-Optics (CLEO)* (2018), pp. 1–2.
22. Z. Wang, C. Chen, K. Wu, H. Chong, and H. Ye, "Transparent Conductive Oxides and Their Applications in Near Infrared Plasmonics," Phys. status solidi **216**(5), 1700794 (2019)..

Optics EXPRESS

23. C. P. Liu, Y. Foo, M. Kamruzzaman, C. Y. Ho, J. A. Zapien, W. Zhu, Y. J. Li, W. Walukiewicz, and K. M. Yu, "Effects of Free Carriers on the Optical Properties of Doped CdO for Full-Spectrum Photovoltaics," Phys. Rev. Appl. **6**(6), 064018 (2016)..
24. U. Koch, C. Hoessbacher, J. Niegemann, C. Hafner, and J. Leuthold, "Digital Plasmonic Absorption Modulator Exploiting Epsilon-Near-Zero in Transparent Conducting Oxides," IEEE Photonics J. **8**(1), 1–13 (2016)..
25. E. Li and A. X. Wang, "Femto-Joule All-Optical Switching Using Epsilon-Near-Zero High-Mobility Conductive Oxide," IEEE J. Sel. Top. Quantum Electron. **27**(2), 1–9 (2021).
26. J. Sun, E. Timurdogan, A. Yaacobi, E. S. Hosseini, and M. R. Watts, "Large-scale nanophotonic phased array," Nature **493**(7431), 195–199 (2013)..
27. R. Amin, J. K. George, S. Sun, T. Ferreira de Lima, A. N. Tait, J. B. Khurgin, M. Miscuglio, B. J. Shastri, P. R. Prucnal, T. El-Ghazawi, and V. J. Sorger, "ITO-based electro-absorption modulator for photonic neural activation function," APL Mater. **7**(8), 081112 (2019)..
28. L. Vertchenko, N. Akopian, and A. V. Lavrinenko, "Epsilon-Near-Zero Grids for On-chip Quantum Networks," Sci. Rep. **9**(1), 6053 (2019)..
29. I. C. Reines, M. G. Wood, T. S. Luk, D. K. Serkland, and S. Campione, "Compact epsilon-near-zero silicon photonic phase modulators," Opt. Express **26**(17), 21594–21605 (2018)..
30. J. Parra, I. Olivares, F. Ramos, and P. Sanchis, "Ultra-compact non-volatile Mach-Zehnder switch enabled by a high-mobility transparent conducting oxide," Opt. Lett. **45**(6), 1503–1506 (2020)..
31. H. Wang, K. Du, C. Jiang, Z. Yang, L. Ren, W. Zhang, S. J. Chua, and T. Mei, "Extended Drude Model for Intraband-Transition-Induced Optical Nonlinearity," Phys. Rev. Appl. **11**(6), 064062 (2019)..
32. E. O. Kane, "Band structure of indium antimonide," J. Phys. Chem. Solids **1**(4), 249–261 (1957)..
33. M. Z. Alam, S. A. Schulz, J. Upham, I. De Leon, and R. W. Boyd, "Large optical nonlinearity of nanoantennas coupled to an epsilon-near-zero material," Nat. Photonics **12**(2), 79–83 (2018)..
34. P. Guo, R. D. Schaller, J. B. Ketterson, and R. P. H. Chang, "Ultrafast switching of tunable infrared plasmons in indium tin oxide nanorod arrays with large absolute amplitude," Nat. Photonics **10**(4), 267–273 (2016)..
35. R. Shaviv, E. F. Westrum, R. J. C. Brown, M. Sayer, X. Yu, and R. D. Weir, "The heat capacity and derived thermophysical properties of the high TC superconductor YBa2Cu3O7−δ from 5.3 to 350 K," J. Chem. Phys. **92**(11), 6794–6799 (1990)..
36. E. Carpene, "Ultrafast laser irradiation of metals: Beyond the two-temperature model," Phys. Rev. B **74**(2), 024301 (2006)..
37. E. Sachet, C. T. Shelton, J. S. Harris, B. E. Gaddy, D. L. Irving, S. Curtarolo, B. F. Donovan, P. E. Hopkins, P. A. Sharma, A. L. Sharma, J. Ihlefeld, S. Franzen, and J.-P. Maria, "Dysprosium-doped cadmium oxide as a gateway material for mid-infrared plasmonics," Nat. Mater. **14**(4), 414–420 (2015)..
38. K. P. Kelley, E. Sachet, C. T. Shelton, and J.-P. Maria, "High mobility yttrium doped cadmium oxide thin films," APL Mater. **5**(7), 076105 (2017)..
39. D. C. Look, K. D. Leedy, A. Kiefer, B. Claflin, N. Itagaki, K. Matsushima, and I. Surhariadi, "Model for thickness dependence of mobility and concentration in highly conductive zinc oxide," Opt. Eng. **52**(3), 033801 (2013)..
40. M. Bache and A. V. Lavrinenko, "Ultrafast nonlinear dynamics of thin gold films due to an intrinsic delayed nonlinearity," J. Opt. **19**(9), 094004 (2017)..
41. H. Wang, K. Du, R. Liu, X. Dai, W. Zhang, S. J. Chua, and T. Mei, "Role of hot electron scattering in epsilon-near-zero optical nonlinearity," Nanophotonics **9**(14), 4287–4293 (2020)..
42. H. Ma, Y. Zhao, Y. Shao, X. Lin, D. Li, Z. Cao, Y. Leng, and J. Shao, "Determining femtosecond laser fluence for surface engineering of transparent conductive thin films by single shot irradiation," Opt. Express **29**(23), 38591–38605 (2021)..
43. B. Sturlesi, M. Grajower, N. Mazurski, and U. Levy, "Integrated amorphous silicon-aluminum long-range surface plasmon polariton (LR-SPP) waveguides," APL Photonics **3**(3), 036103 (2018).